

1. Projected equations

In this section, we will show that the system of equations (2.5) which govern the dynamics of the perturbations can be written in the classical state-space form presented in Eq. (5.2).

Equation (2.5) can first be recast in the form

$$\begin{pmatrix} \mathbf{M} & 0 \\ 0 & 0 \end{pmatrix} \frac{d}{dt} \begin{pmatrix} \mathbf{u}' \\ p' \end{pmatrix} = \begin{pmatrix} \mathbf{A}_1 & \mathbf{A}_2^* \\ \mathbf{A}_2 & 0 \end{pmatrix} \begin{pmatrix} \mathbf{u}' \\ p' \end{pmatrix} + \begin{pmatrix} \mathbf{M}\mathbf{f}' \\ 0 \end{pmatrix}, \quad (1.1)$$

where \mathbf{u}' denotes the velocity field and p' stands for the corresponding pressure field. We now reformulate the above equations into standard state-space form. To this end we multiply the momentum equation by $\mathbf{A}_2\mathbf{M}^{-1}$, which yields — assuming that $\mathbf{A}_2\dot{\mathbf{u}}' = 0$ — an expression for the pressure in terms of the velocity field

$$p' = -(\mathbf{A}_2\mathbf{M}^{-1}\mathbf{A}_2^*)^{-1} [(\mathbf{A}_2\mathbf{M}^{-1}\mathbf{A}_1) \mathbf{u}' + \mathbf{A}_2\mathbf{f}']. \quad (1.2)$$

This relation can be used to eliminate the explicit divergence constraint and allows us to write the governing linearized equations in the desired form

$$\frac{d\mathbf{u}'}{dt} = \mathbf{Z}\mathbf{A}_1\mathbf{u}' + \mathbf{Z}\mathbf{M}\mathbf{f}', \quad (1.3)$$

where

$$\mathbf{Z}\mathbf{M} = \mathbf{I} - \mathbf{M}^{-1}\mathbf{A}_2^*(\mathbf{A}_2\mathbf{M}^{-1}\mathbf{A}_2^*)^{-1}\mathbf{A}_2 \quad (1.4)$$

is the projection matrix onto the divergence-free space. Note that if \mathbf{u}' is already divergence free, we have $\mathbf{Z}\mathbf{M}\mathbf{u}' = \mathbf{u}'$.

Defining $\tilde{\mathbf{A}} = \mathbf{Z}\mathbf{A}_1$ and $\tilde{\mathbf{M}} = \mathbf{Z}\mathbf{M}$, Eq. (1.3) is the same as Eq. (5.2) of the article.

2. Effect of discretization order on eigen-spectrum and ϵ -pseudo-spectrum

We briefly analyze here the influence of the discretization order. We have represented for this in figure 1(a) the eigenspectrum obtained in the case of disc. D_3 , which displays the same mesh as in D_1 but a higher spatial discretization order. We can see that the spectrum is qualitatively similar to the one shown in figure 7(a) of the article, with the damping rates of the high frequency non-overlapping eigenvalues remaining approximately near $-\sigma \approx 15$. Figure 1(b) shows a comparison of the "background" value of ϵ obtained for discs. D_1, D_2, D_3 and D_4 along $\omega = 20$ and $\omega = 80$. We can see that the values obtained for the first-order spatial discretization (D_1) are very close to those obtained for the second-order discretization (D_3) for both frequencies. This shows that ϵ is a robust quantity with respect to numerical choices: a region of quasi-eigenvalues remains as such when changing the order of the spatial discretization.

3. Eigenvalues in region where $\epsilon < 10^{-12}$

To further illustrate the meaning of a region displaying $\epsilon < 10^{-12}$, we check that the eigenvalues computed by our numerical method in such a region are "true" eigenvalues, in the sense that a linearized DNS code initialized by the real part of an eigenmode yields a solution whose time-behavior is consistent with its eigenvalue μ . Note first that we verified a posteriori that all eigenvalues reported in figures 7(a,b,c) of the article and in figure 1(a) satisfied $\|\mathbf{A}\hat{\mathbf{q}} - \mu\mathbf{B}\hat{\mathbf{q}}\|_2 / \|\mu\mathbf{B}\hat{\mathbf{q}}\|_2 \leq 5 \cdot 10^{-11}$, where $\|\cdot\|_2$ refers to the classical vector 2-norm. This shows that all computed eigenvalues are eigenvalues nearly up to

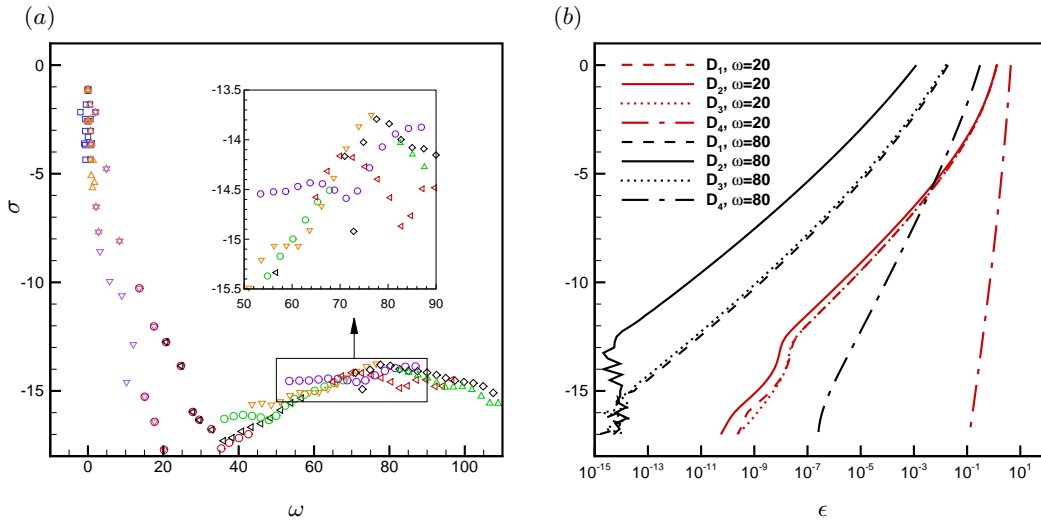


FIGURE 1. (a) - Eigenvalue spectrum in the (ω, σ) -plane obtained for disc. D_3 . Colors indicate eigenvalues computed with distinct shift parameters s (see figure 7(b) of the article). (b) - Comparison of ϵ between discs. D_1, D_2, D_3 and D_4 along $\omega = 20$ and $\omega = 80$. $Re = 1600$. In plot (a), the inset corresponds to the same inset as the one in figure 7(a) of the article.

machine precision. Second, we have ascertained that time-marching the linearized Navier-Stokes equations by solving Eq. (4.2) of article at each time-step (with $\mathbf{f}^m = 0$) also agrees with the eigen-computations. We checked this by considering several eigenvalues obtained in the overlapping region. For example, figure 2 is concerned with the eigenvalue $\mu = -15.0 + 61.4i$, for $Re = 1600$ and disc. D_1 . We can see that the temporal u_z -signal given at point $(r_c = 0.9, z_c = 8)$ by the linearized DNS (initialized by the real part of the eigenmode) fully agrees with the signal deduced from the eigenvalue and the structure of the eigenmode. Such results are in agreement with those of Chedevigne *et al.* (2012); Boyer *et al.* (2013) who performed a similar check.

4. Spatial convergence and sensitivity to location of left and right boundaries

We have represented in figure 3(a) a comparison of the leading optimal gain λ_1 , given respectively by discs. D_1, D_2, D_3 and D_4 as a function of ω . In figure 3(b), we have compared the axial density functions of the leading optimal forcing and response at $\omega = 62.5$ for all discretizations. From these results, we may conclude that, if the head-end is included in the computational domain, then the location of the outlet boundary and of the precise outlet boundary condition has no influence on the optimal gain (figure (a)), on the optimal forcing (figure (b)) and on the optimal response within the optimization region $z \leq 8$ (figure (b)). On the other hand, if the computational domain starts at $z_b = 4$, both the optimal forcing and response may be heavily changed, especially for frequencies satisfying $\omega < 80$, for which the optimal forcing is located within $z < 4$. This has been exemplified in figure (b) for $\omega = 62.5$ where the leading optimal forcing and response for disc. D_4 have been compared to the structures obtained for $z_b = 0$ (disc. D_1): it is seen that the removal of region $z < 4$ strongly impacts the amplification potential at this frequency.

Comparing first- (D_1) and second-order (D_3) discretizations, we can conclude that the

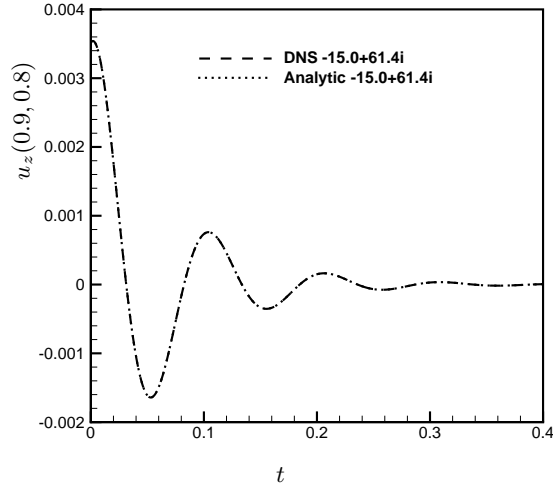


FIGURE 2. Comparison between linearized DNS signal $u_z(r_c, z_c, t)$ and analytic prediction $e^{\sigma t}(\hat{u}_z^r(r_c, z_c) \cos \omega t - \hat{u}_z^i(r_c, z_c) \sin \omega t)$ for eigenvalue $\mu = -15.0 + 61.4i$ and spatial location near the injecting wall ($r_c = 0.9, z_c = 8$). $Re = 1600$ and disc. D_1 .

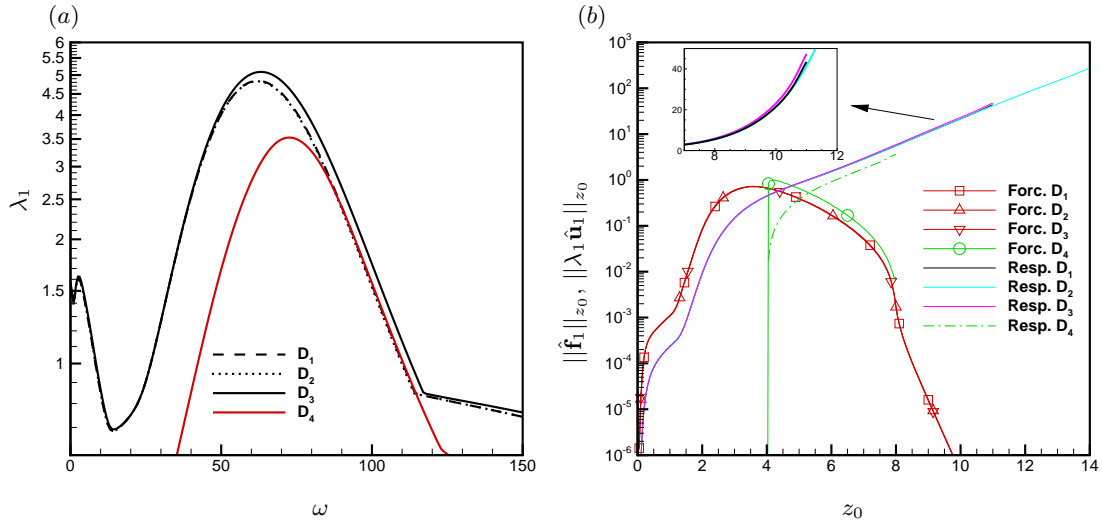


FIGURE 3. (a) - Leading optimal gain for discs. D_1, D_2, D_3 and D_4 . (b) - Axial energy density function of leading optimal forcing and response at $\omega = 62.5$. $Re = 1600$.

optimal forcings are converged (figure 3(b)), but that the optimal gains and responses are slightly underestimated with a first-order discretization (figures (a,b)), especially for high-frequencies where the optimal responses display small-scale structures.

REFERENCES

- BOYER, G., CASALIS, G. & ESTIVALÈZES, J. L. 2013 Stability and sensitivity analysis in a simplified solid rocket motor flow. *J. Fluid Mech.* **722**, 618–644.
- CHEDEVERGNE, F., CASALIS, G. & MAJDALANI, J. 2012 Direct numerical simulation and

biglobal stability investigations of the gaseous motion in solid rocket motors. *J. Fluid Mech.* **706**, 190–218.